



# The Influence of Nominal Composition on the Microstructure, Tensile Properties, and Weldability of Cast Monel Alloys

CHRISTOPHER J. FARNIN, ERIC N. COKER, PERLA A. SALINAS,  
and JOHN N. DUPONT

Cast Monel alloys are used in many industrial applications that require a combination of good mechanical properties and excellent resistance to corrosion. Despite relative widespread use, there has been limited prior research investigating the fundamental composition–structure–property relationships. In this work, microstructural characterization, thermal analysis, electron probe microanalysis, tensile testing, and Varestraint testing were used to assess the effects of variations in nominal composition on the solidification path, microstructure, mechanical properties, and solidification cracking susceptibility of cast Monel alloys. It was found that Si segregation caused the formation of silicides at the end of solidification in grades containing at least 3 wt pct Si. While increases to Si content led to significant improvements in strengthening due to the precipitation of  $\beta_1$ -Ni<sub>3</sub>Si, the silicide eutectics acted as crack nucleation sites during tensile loading which severely reduced ductility. The solidification cracking susceptibility of low-Si Monel alloys was found to be relatively low. However, increases to Si concentration and the onset of associated eutectic reactions increased the solidification temperature range and drastically reduced cracking resistance. Increases in the Cu and Mn concentrations were found to reduce the solubility limit of Si in austenite which promoted additional eutectic formation and exacerbated the reductions in ductility and/or weldability.

<https://doi.org/10.1007/s11661-023-07269-5>

© The Minerals, Metals & Materials Society and ASM International 2023

## I. INTRODUCTION

MONEL alloys are used in many industrial applications requiring good mechanical properties and excellent resistance to corrosion. The ASTM A494 specification defines the compositions of several cast grades that span a range of Si and Nb concentrations and impart changes to the microstructure and subsequent properties of the alloys.<sup>[1]</sup> These materials are commonly fabricated, repaired, and joined through solidification processes like casting and fusion welding, and thus have properties that are highly dependent on the nominal composition, solidification behavior, and concomitant solidified microstructure.

Despite frequent use in industry, there is limited prior research investigating the influence of nominal composition on the microstructure, tensile properties, and

weldability of cast Monel alloys. Sahoo *et al.* assessed the tensile properties of cast Monels with systematic variations in Si and Nb concentration.<sup>[2]</sup> It was found that both elements contributed significantly to strengthening and that the alloys spanned a wide range of properties depending on composition. Yield strength was found to vary from 176 to 560 MPa, ultimate tensile strength (UTS) from 380 to 854 MPa, and elongation from 50 to 8 pct. However, the authors did not perform sufficient microstructural characterization or fractography to make definitive correlations between composition, microstructure, and properties.<sup>[2]</sup>

Eash and Kihlgren also performed tensile testing on a series of Monel alloys with variations in composition and found similar results.<sup>[3]</sup> Yield strength was found to be highly sensitive to Si concentration and UTS increased to a slightly lesser extent.<sup>[3]</sup> Although beneficial for strengthening, the ductility was significantly reduced at higher Si contents. The authors attributed the strengthening effects to an increase in solid-state silicide precipitation, but did not comment on the mechanism responsible for the reductions in ductility. A recent study by Wang *et al.* proposed that increased amounts of Si-rich eutectic constituents were responsible for lowered tensile elongation, but no direct evidence was

CHRISTOPHER J. FARNIN and JOHN N. DUPONT are with the Lehigh University, 5 E Packer Ave, Bethlehem, PA 18015. Contact e-mail: [cjf219@lehigh.edu](mailto:cjf219@lehigh.edu) ERIC N. COKER and PERLA A. SALINAS are with the Sandia National Laboratories, P.O. Box 5800, Albuquerque, NM 87185.

Manuscript submitted July 30, 2023; accepted November 18, 2023.

Article published online December 15, 2023

provided to support the claim, and no quantitative relationships between microstructure and properties were identified.<sup>[4]</sup>

With respect to weldability, low-Si Monel castings and wrought counterparts have been shown to be readily weldable and exhibit low susceptibility to solidification cracking relative to many other commercial Ni-base alloys.<sup>[5–8]</sup> There have been no studies assessing the weldability of the medium or high-Si Monel grades such as M30H or M25S. The ASTM A494 standard notes that these alloys are unable to be weld repaired, but two anecdotal reports claimed that M30H, which contains ~ 3 wt pct Si, could be successfully welded under proper conditions.<sup>[9,10]</sup> However, no experimental evidence was presented. Microstructural characterization of these grades and related Ni–Cu–Si alloys have revealed that silicide phases formed in the interdendritic regions during solidification.<sup>[3,4,11]</sup> The formation of similar Si-rich intermetallics, such as Laves and G phase, have been shown to be highly detrimental to the solidification cracking susceptibility of other Si-bearing Ni-base alloys such as HR-160, by extending the solidification temperature range.<sup>[12–14]</sup> The effect of changes to other alloying elements in the system such as Fe, Mn, and Cu on the microstructure and properties have not been investigated in any prior studies.

Despite the well-documented influences of solute concentration on the properties of Monel alloys and other similar systems, the fundamental composition–microstructure–property relationships of cast Monel alloys have not been well established. In particular, the metallurgical mechanisms responsible for the reported changes to behavior require further investigation. The objective of this work was thus to investigate how broad changes to composition, including variations in Si, Nb, and Cu concentration, influence the solidification path, microstructure, tensile properties, and solidification cracking susceptibility of cast Monel alloys.

## II. PROCEDURE

The compositions of the alloys studied in this work are listed in Table I. Each alloy was fabricated by

melting virgin elements under an Ar atmosphere, heating to 1550 °C to produce a homogenous melt, and then casting into a zirconia coated graphite mold with internal dimensions of 6" × 15" × 2". The melt was poured into the 2" × 6" face of the mold and no mold preheat was applied. Samples were cut from near the center of each casting, mounted in conductive polymer, metallographically prepared to a final polish of 0.05 μm, and etched using ASTM Etchant No. 38.<sup>[15]</sup> Characterization of the cast microstructures was performed *via* imaging with a Hitachi-4300 field emission scanning electron microscope (SEM). Phase fraction measurements were performed by thresholding images collected from as-polished samples of each alloy using the ImageJ/FIJI software.<sup>[16]</sup> X-ray diffraction (XRD) was performed on samples prepared from each alloy over a 2θ interval of 20 to 110 deg with a step size of 0.013 deg. To prevent texturing effects caused by grain anisotropy, samples for XRD were ground into a powder using a 65 HRC metal file. Electron probe microanalysis (EPMA) was conducted using a JXA-8900 SuperProbe with an accelerating voltage of 15 kV, current of 30 nA, and working distance of 11 mm. The Probe for EPMA software was used to convert X-ray counts into concentrations after standardization on a series of pure element standards.<sup>[17]</sup> Phase compositions were reported as an average of at least eight measurements. To characterize solute segregation within the austenitic matrices, 16 × 16 grids of EPMA measurements were taken with a 200 μm point spacing. Solute concentration profiles were then assembled using the weighted interval rank sort (WIRS) technique developed by Ganesan *et al.*<sup>[18]</sup> Solute partition coefficients (*k*) were calculated using the EPMA data and a Scheil analysis using a procedure outlined in prior work.<sup>[18]</sup> Concentration profiles were graphed in accordance with Eq. [1], a linear fit was applied to the data, and the slope of the trendline was used to calculate *k*.<sup>[18]</sup>

$$\ln(C_s) = (k - 1)\ln(1 - f_s) + \ln(kC_0), \quad [1]$$

where  $C_s$  is solid concentration,  $C_0$  is the nominal concentration, and  $f_s$  is the fraction solid. The use of this procedure assumes that the alloys solidified under non-equilibrium conditions where there was negligible

**Table I. Nominal Compositions of the Cast Monel Alloys Used in this Study**

Alloy	Description	Ni	Cu	Fe	Si	Nb	Mn	C	Al	V
1	high Si, low Nb	fill	30.29	3.38	4.41	0.50	1.48	0.31	0.04	—
2	med. Si, low Nb	fill	30.33	3.57	2.98	0.51	1.52	0.33	0.03	—
3	low Si, low Nb	fill	29.94	3.57	1.08	0.51	1.53	0.32	0.03	—
4	med. Si, med. Nb	fill	29.31	3.48	2.94	1.42	1.50	0.31	0.04	—
5	high Si, high Nb	fill	29.66	3.45	4.42	2.70	1.52	0.30	0.05	—
6	low Si, high Nb	fill	29.69	3.58	1.07	2.76	1.52	0.32	0.04	—
7	med. Si, high Nb	fill	29.65	3.50	2.90	2.60	1.50	0.32	0.04	—
8	highest Cu, med. Si	fill	60.19	3.68	2.95	1.48	1.50	0.30	0.06	—
9	high Cu, med. Si	fill	45.32	3.59	3.00	1.49	1.54	0.32	0.04	—
10	V, med. Si	fill	29.61	3.50	2.95	1.32	1.47	0.31	0.04	0.45
11	high Mn	fill	30.09	3.53	2.96	1.90	9.84	0.32	0.04	—

All values are shown in wt pct.

diffusion in the solid phase, infinite diffusion in the liquid phase, equilibrium at the solid–liquid interface, and no dendrite tip undercooling. These assumptions will be validated in the subsequent section. Differential scanning calorimetry (DSC) was performed using a Netzsch STA 449F3 Jupiter Thermal Analyzer on 180 mg samples cut from the castings immediately adjacent to the samples removed for microstructural characterization. Each sample was heated in a high purity alumina cup with pin-hole lid to a peak temperature of 1315 °C or 1375 °C (depending on the expected melting temperature) at 10 °C/min and then cooled at the same rate in an atmosphere of flowing Ar. Phase transition temperatures were taken at the deviation from the local baseline. Additional details on the characterization procedures can be found elsewhere.<sup>[19]</sup>

Vickers microhardness testing was performed on as-polished samples using a Leco LM-248 AT Microhardness Tester. Grids of 16 × 16 indents were placed on each alloy using a load of 100 gf and an indenter dwell time of 10 seconds. A point spacing of 88 μm was selected to place the indents as close together as possible while maintaining the minimum required spacing outlined in the ASTM E384 specification.<sup>[20]</sup> Room temperature tensile testing was performed on 0.35" diameter cylindrical dog-bone samples machined from defect free areas of the cast blocks in accordance with ASTM E8.<sup>[21]</sup> The samples were pulled with a crosshead speed of 0.005 in./min up until yielding occurred, then at 0.4 in./min. until failure. The yield strength, UTS, and percent elongation were reported as the average of two tests from each alloy. The fracture surfaces of the tensile samples were examined in the SEM. Secondary cracking directly below the fracture surface was characterized by bisecting the fracture surfaces, metallographically preparing them to produce a transverse, edge-on view beneath the surface, and imaging in the SEM.

Longitudinal Vareststraint testing was performed on at least three test bars (165 mm × 25 mm × 6 mm) machined from each alloy.<sup>[22]</sup> Autogenous gas tungsten arc welding (GTAW) was performed along the lengths of each bar with a current of 175 A, voltage of 12 V, and travel speed of 2 mm/s, using Ar shield gas. The parameters were selected to achieve adequate

penetration through the 6mm thickness of the bars. Near the end of the welding process, the bars were bent over a die block by a pneumatic arm to induce an augmented bending strain of 2.1 pct over the solidifying weld. Samples of wrought 304L stainless steel were tested for reference as it is known to have very low susceptibility to solidification cracking.<sup>[23]</sup> The maximum crack length (MCL) within the fusion zone (FZ) of each bar was measured using a Nikon AZ100 stereomicroscope. SEM imaging was performed on metallographically prepared samples cut from cracked regions of the test bars.

### III. RESULTS AND DISCUSSION

#### A. Effect of Si and Nb on Cast Microstructure and Solidification Path

Table I lists the compositions of the alloys examined in this work. Alloys 1–7 contain differences in Si and Nb concentrations that span the ranges defined in the ASTM A494 specification.<sup>[1]</sup> Both elements were systematically varied at low, medium, and high levels such that the individual and coupled behaviors of each element could be resolved.

The effects of Si and Nb concentration on the microstructure and solidification path of cast Monel alloys have been described in detail in a previous article, and are summarized here in support of the mechanical property and weldability results.<sup>[19]</sup> The microstructure of Alloy 4, containing intermediate Si and Nb concentrations of 3 and 1.4 wt pct, respectively, is shown in Figure 1. The microstructure consisted of an austenitic matrix, with groupings of primary, faceted NbC particles, and small amounts of graphite. Several distinct Ni–Si intermetallic phases were also observed within eutectic constituents and in nanoscale precipitates (although the term eutectic is used here, it is acknowledged that the constituents formed in a multicomponent system and thus do not represent a true binary eutectic reaction). The most prevalent of the two intermetallic eutectic constituents was identified as Ni<sub>31</sub>Si<sub>12</sub> via EPMA composition measurements and XRD scans on higher-Si alloys that contained the same phase. The

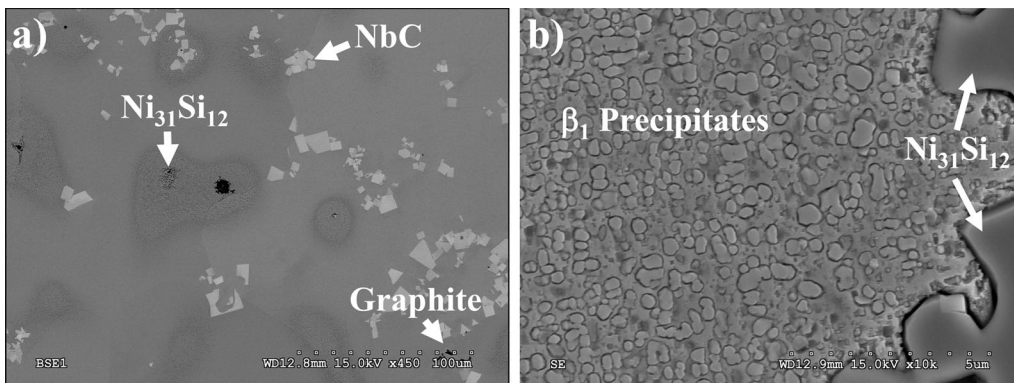


Fig. 1—SEM micrographs showing the microstructure of Alloy 4 containing intermediate Si and Nb concentrations at (a) low magnification, and (b) high magnification.

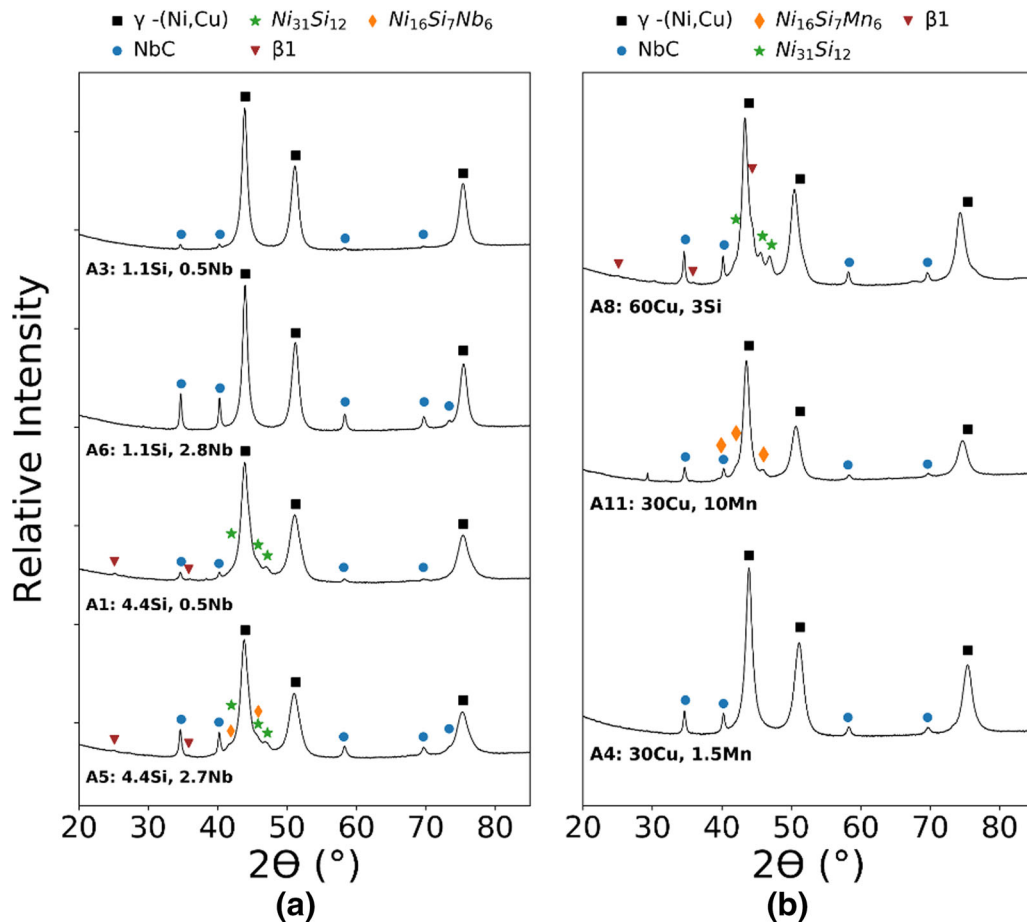


Fig. 2—Diffractograms showing (a) the effects of Si and Nb concentration (Alloys 3, 6, 1, and 5), and (b) the effects of Cu and Mn concentration (Alloys 8, 11, and 4) on the phases formed within the cast microstructures.

XRD data for several alloys are shown in Figure 2(a); however, the eutectic constituents in Alloy 4 were not present in sufficient quantity to resolve in the diffractograms. Table II lists the composition of another intermetallic constituent that was found in Alloys 2 and 4 in very small amounts. The measured EPMA compositions of that phase were in close agreement with the expected stoichiometry of  $\beta_1$ -Ni<sub>3</sub>Si.<sup>[24]</sup> Figure 1(b) shows  $\beta_1$  precipitates that formed in the solid-state during cooling from casting. They were found extensively throughout the interdendritic regions where the Si concentration was measured to be locally enriched. Changes in Nb concentration among the 3 wt pct Si alloys (Heats 2 and 7) did not have a significant effect on intermetallic formation, but did alter the relative phase fractions of NbC and graphite.

Figure 3(a) shows that among Alloys 1–7, lower Nb concentrations reduced the volume fraction of NbC, which was generally present with a script morphology, while promoting the formation of graphite. Increasing Nb concentration up to ~ 2.7 wt pct eliminated graphite from the microstructure and promoted primary NbC formation in quantities of ~ 3 vol pct. Figure 3(b) shows that when Si concentration was reduced to 1 wt pct, as in Alloys 3 and 6, the silicide eutectic constituents did not form. Elevations in Si content, as in Alloys 1 and 5,

resulted in higher fractions of the constituents. While no eutectic  $\beta_1$  was observed in the high-Si variants, an additional Ni–Si–Nb intermetallic was found within the eutectic constituents in Alloy 5 in small amounts. The EPMA measured composition of that phase is listed in Table II, and it was identified as G phase (Ni<sub>16</sub>Si<sub>7</sub>Nb<sub>6</sub>).

DSC testing was performed on each alloy to determine how composition affected the solidification path and phase transition temperatures and the results are catalogued in Table III. The liquidus temperatures ( $T_L$ ) of Alloys 1–7, which varied from 1214 °C to 1310 °C, did not change as a function of Nb concentration, but decreased linearly with nominal Si concentration ( $C^{Si}$ ) according to a line of best fit described by Eq. [2].

$$T_L = -27.33C^{Si} + 1339.30, \quad r^2 > 0.99. \quad [2]$$

At temperatures just below  $T_L$ , several alloys showed small peaks or inflection points corresponding to the formation of secondary NbC and/or graphite. These peaks were not resolvable in some alloys due to the low phase volume fractions and corresponding formation enthalpies. In the medium and high-Si alloys, solidification was found to terminate with a  $L \rightarrow \gamma + \text{Ni}_{31}\text{Si}_{12}$  eutectic reaction, as low temperature exotherms present in the on-cooling (OC) data had areas that correlated



Table II. Compositions of Intermetallic Phases Measured via EPMA

Phase	Ni	Cu	Si	Fe	Mn	Nb	Measured Stoichiometry	Measured Alloys
Ni <sub>31</sub> Si <sub>12</sub>	68.37 ± 1.17	2.75 ± 0.78	27.39 ± 0.79	1.00 ± 0.87	0.47 ± 0.05	0.02 ± 0.01	A <sub>31.22</sub> B <sub>11.78</sub> A = (Ni, Cu, Fe, Mn, Nb) B = Si	1, 2, 4, 5, 8, 9, 10
Ni <sub>3</sub> Si (β <sub>1</sub> )	69.47 ± 0.31	6.30 ± 0.34	22.18 ± 0.09	1.04 ± 0.12	0.98 ± 0.01	0.02 ± 0.01	A <sub>3.05</sub> B <sub>0.95</sub> A = (Ni, Cu, Fe) B = (Si, Fe, Mn, Nb)	2, 4
Ni <sub>16</sub> Si <sub>7</sub> Nb <sub>6</sub> (G Phase)	57.33	2.58	24.59	0.99	2.64	11.86	A <sub>16.63</sub> B <sub>7.13</sub> C <sub>5.24</sub> A = Ni, B = Si C = (Nb, Mn, Cu, Fe)	5
Ni <sub>16</sub> Si <sub>7</sub> Mn <sub>6</sub> (G Phase)	56.36	4.61	22.90	0.82	15.28	0.03	A <sub>16.34</sub> B <sub>6.64</sub> C <sub>6.01</sub> A = Ni, B = Si C = (Nb, Mn, Cu, Fe)	11

All values are shown in at. pct. Stoichiometries of β<sub>1</sub> and G phase were estimated using guidance from literature.<sup>[45,54]</sup>

with the measured eutectic fractions from the castings. This reaction was not resolvable in Alloys 4 or 7 due to the low volume fraction, but was measured to occur between 1043 °C and 1055 °C in the remaining eutectic-bearing alloys. The Nb concentration did not have a discernable effect on the liquidus or eutectic temperatures.

The solidification temperature range (STR) of each alloy was calculated by taking the difference between the on-heating (OH)  $T_L$  and the onset of the  $\gamma/\text{Ni}_{31}\text{Si}_{12}$  eutectic reaction ( $T_e$ ) on-cooling (OC). The OH  $T_L$  values were utilized because they were not dependent on undercooling effects, and would be more representative of the behavior during welding in which solidification occurs epitaxially from pre-existing base metal grains without undercooling. Depending on Si concentration, the STR was estimated to vary from 164 °C to 216 °C, which is high compared to other Ni-base alloys.<sup>[12,25]</sup> The STR of the low-Si heats (Alloys 3 and 6) could not be measured, as terminal reaction exotherms could not be clearly determined from the data. The STR of these heats was expected to be much lower, since microstructural characterization revealed that solidification terminated with either  $\gamma/\text{NbC}$  or  $\gamma/\text{graphite}$  reactions which were measured to occur at temperatures much greater than  $T_e$  in the other alloys.

To gain a better understanding of how solute segregation during the solidification process influenced the solidification path and formation of silicide eutectic constituents, solid concentration profiles for each element were created using sorted EPMA data. Example profiles for the distribution of Si between the dendrite core and interdendritic regions are shown for Alloys 1–7 in Figure 4. The large concentration gradients across the microstructures were characteristic of non-equilibrium solidification. Prior calculations of the dimensionless diffusion parameter ( $\alpha$ ) for Si in Alloy 2 verified that solid-state diffusion was negligible during the casting process and validated the non-equilibrium condition.<sup>[19]</sup> Silicon was shown to segregate strongly to the liquid in the medium and high-Si grades and approached similar concentrations in the interdendritic region corresponding to the maximum solid solubility limit of Si in the austenitic matrix. This value was measured to be  $4.99 \pm 0.21$  wt pct by empirically fitting the concentration profiles of the medium and high-Si grades to polynomial curves and using the equations to determine the interdendritic concentrations at high- $f_s$  values. The EPMA and DSC results indicated that excess Si remaining in the liquid after the solubility limit was reached led to the  $\gamma/\text{Ni}_{31}\text{Si}_{12}$  eutectic reaction. The concentration profiles for the 1 wt pct Si alloys maintain relatively low concentrations across the entire dendrite arm due to the low nominal Si concentration and did not reach the solubility limit which was consistent with the lack of silicide eutectic constituents found within the microstructures.

Solute partition coefficients, defined as the ratio of the concentration of solute in the solid phase ( $C_s$ ) and liquid phase ( $C_L$ ) at a fixed temperature, were calculated for each element to quantify the magnitude and direction of segregation. The  $k$  values for Alloys 1–7 are listed in

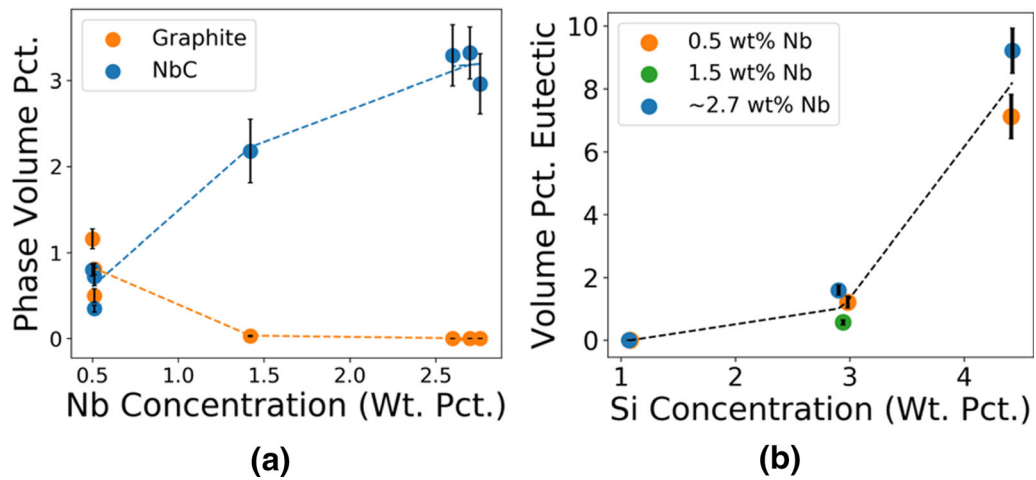


Fig. 3—(a) The effects of Nb concentration on the fraction graphite and NbC, and (b) the effect of Si content on the fraction eutectic in Alloys 1–7. Error bars represent the standard error of the measurements. Adapted from Ref. [19].

Table IV and are generally consistent between each grade, showing that variations in Si and Nb concentration did not significantly change the partitioning behavior of most elements. Silicon, Mn, and Cu segregated to the liquid during solidification, while Ni and Fe partitioned to the solid. Most of the  $k$  values were shown to agree with the results of prior studies in literature, apart from  $k^{\text{Cu}}$  which was measured to be higher than the value of 0.78 found in welds of Monel 400, and thus segregated less significantly.<sup>[26]</sup> The measurement of Nb segregation was complicated by low matrix concentrations and scatter within the data which prevented the calculation of  $k^{\text{Nb}}$  in some alloys. The partitioning behavior of Nb was found to depend on composition as  $k^{\text{Nb}}$  decreased from 1.20 to 0.96 as Si concentration was increased from 1.1 to 4.4 wt pct in the high-Nb heats. The decrease in  $k^{\text{Nb}}$ , and elevated liquid concentration near the end of solidification in Alloy 5, was consistent with the formation of the Nb-rich G Phase in that alloy. Niobium has historically been shown to segregate strongly to the liquid during solidification in most Ni-base alloys which is markedly different than the behavior observed in the Monel alloys.<sup>[27,28]</sup> Solidification modeling performed in a prior work suggested that the solid phase-partitioning of Nb in the Monel system related to the high nominal Cu concentration and the segregation of Cu to the liquid phase during solidification.<sup>[19]</sup>

### B. Effect of Cu on Cast Microstructure and Solidification Path

Alloys 9 and 8 have comparable compositions to Alloy 4, but with increases in Cu concentration to investigate the effects of Cu at three levels. The microstructures of the high-Cu alloys are shown in Figure 5 and have many similarities with Alloy 4. Both alloys contained primary, faceted NbC particles, graphite, micro/nanoscale precipitates, and Si-rich eutectic constituents. EPMA composition measurements on the intermetallic eutectic constituents were consistent with  $\text{Ni}_{31}\text{Si}_{12}$  as shown in Table II. This was supported by the

XRD data displayed in Figure 2(b), which showed more pronounced characteristic peaks for  $\text{Ni}_{31}\text{Si}_{12}$  with increasing Cu concentration. Small peaks consistent with  $\beta_1$  were also observed. Figure 6 shows the quantitative relationships between Cu concentration and the phase fractions of eutectic, NbC, and graphite. Despite the fixed Si content of 3 wt pct in all alloys, the measured eutectic fraction increased linearly from 0.6 to 10.6 vol pct as Cu concentration increased. While there was no significant change in the amount of NbC, the fraction graphite increased from < 0.1 to 0.7 vol pct.

The images in Figures 1 and 5 reveal differences in the precipitates observed throughout the microstructures of the three alloys. Alloy 4 contained a large gradient in the distribution and size of  $\beta_1$  precipitates between the dendrite core and interdendritic regions that was attributed to the large differences in Si concentration and extent of supersaturation with the matrix. The increase in Cu in Alloy 9 resulted in a more moderate gradient, while the further increase in Alloy 8 produced a nearly homogenous dispersion of precipitates throughout the microstructure. A noticeable deviation in precipitate morphology was also observed. Figure 1 shows that the  $\beta_1$  particles in the 30 wt pct Cu alloy had low aspect ratios, with roughly spherical or cubic morphologies depending on size and location along the dendrite arm. In Alloy 9, a mix of spherical and more elongated particles were observed, and in Alloy 8, the precipitates appeared needle-like and had distinct directional orientations. Changes in precipitate morphology are well known to relate to differences in the lattice misfit between the precipitate and matrix; however, the origin of the variations in the Monel alloys was not clear.<sup>[30,31]</sup> The intermetallic phases within the eutectic constituents in Alloys 8 and 9 were previously identified as  $\text{Ni}_{31}\text{Si}_{12}$ , suggesting that the precipitate phase in the higher-Cu alloys was still  $\beta_1$  based on the small characteristic peaks in the XRD data. However, as has been noted in previous work, other silicide phases such as  $\text{Ni}_2\text{Si}$  have very similar peak locations to  $\text{Ni}_{31}\text{Si}_{12}$  and cannot be ruled out as having formed.<sup>[4]</sup> The  $\text{Ni}_2\text{Si}$  phase has been documented to form *via* solid-state reactions in Monel

**Table III. DSC Measured Phase Transformation Temperatures and Solidification Temperature Ranges (STRs) for Each of the Monel Alloys**

Alloy	Description	L → L + γ OH (°C)	L → L + γ OC (°C)	L → L + γ + NbC OC (°C)	L → L + γ + Gra- white OC (°C)	L → γ + Ni <sub>3</sub> Si <sub>12</sub> OC (°C)	L → γ + G Phase OC (°C)	STR (°C)	Precipitate Solvus Tem- perature (°C)
1	high Si, low Nb	1214	—	—	1175	1050	—	164	897
2	med. Si, low Nb	1252	1226	—	1194	1043	—	209	—
3	low Si, low Nb	1310	—	—	—	—	—	—	—
4	med. Si, med. Nb	1265	—	—	—	—	—	216*	—
5	high Si, high Nb	1224	—	—	—	1055	1055**	169	897
6	low Si, high Nb	1309	—	—	—	—	—	—	—
7	med. Si, high Nb	1260	—	—	—	—	—	211*	—
8	highest Cu, med. Si	1147	—	—	—	1030	—	117	868
9	high Cu, med. Si	1207	—	—	—	1036	—	171	878
10	V, med. Si	1262	—	—	—	1026	—	236	—
11	high Mn	1174	—	—	—	—	989	185	—

\*STR was estimated using the average L → γ + Ni<sub>3</sub>Si<sub>12</sub> from Alloys 1, 2, and 5; \*\*, G Phase, and Ni<sub>3</sub>Si<sub>12</sub> appeared to form simultaneously, or in close succession in Alloy 5.

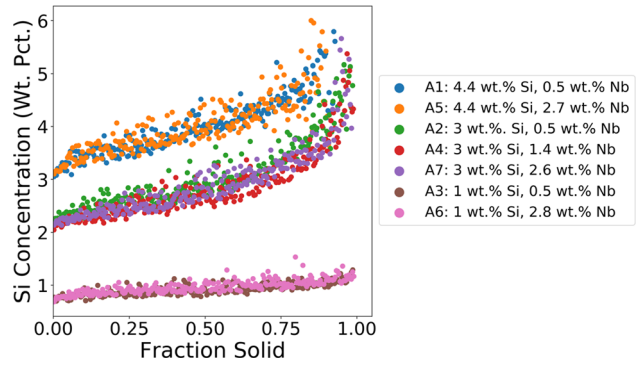


Fig. 4—Silicon solid concentration profiles in Alloys 1–7 measured using EPMA and sorted using the WIRS scheme. Adapted from Ref. [19].

alloys and other Cu-rich alloys containing appreciable Si.<sup>[11,32–34]</sup>

The on-cooling DSC curves for Alloys 4, 9, and 8 are shown in Figure 7 with the corresponding the phase transition temperatures listed in Table III. As Cu concentration ( $C^{Cu}$ ) was increased from 30 to 60 wt pct among those alloys,  $T_L$  was found to decrease linearly by 118 °C in accordance with a line of best fit defined by Eq. [3].

$$T_L = -3.82C^{Cu} + 1377.90, \quad r^2 > 0.99. \quad [3]$$

The liquidus depression was slightly greater than the 89 °C reduction observed over the same Cu interval in the Ni–Cu binary phase diagram generated using Thermo-Calc and the TCBDIN database.<sup>[35,36]</sup> While the terminal  $\gamma/Ni_{31}Si_{12}$  reaction temperature was not detectable in Alloy 4, peaks were identified in results for Alloys 8 and 9 at 1030 °C and 1036 °C, respectively. These were comparable to the  $T_e$  of 1043 °C measured in Alloy 2 which also contained 30 wt pct Cu and 3 wt pct Si, suggesting that Cu had minimal influence over the transformation temperature. Due to the greater effects on  $T_L$ , the STR was found to decrease from ~ 216 °C to 117 °C as Cu content increased from 30 to 60 wt pct.

At lower temperatures beneath  $T_e$ , broad peaks were clearly resolvable above the background starting at 878 °C and 868 °C in Alloys 9 and 8, corresponding to the solid-state precipitation of the silicides. The precipitation onset temperatures could not be readily compared to any of the 30 wt pct Cu, 3 wt pct Si alloys, as peaks were not detected in the on-cooling data for those heats.

Table IV lists the partition coefficients for solute elements in each of the three alloys with varying Cu concentration. The segregation behavior of Ni, Cu, Fe, and Mn were generally observed to be independent of the nominal Cu content. However, the partition coefficients for Si were observed to vary. The full effects of Cu concentration on the segregation behavior of Si can be observed in the solute concentration profiles in Figure 8. Alloys 4 and 9 (with 30 and 45 wt pct Cu, respectively) were measured to have nearly equivalent  $k^{Si}$  values and concentration profiles across most of the solidification interval. The matrix concentration profile for Alloy 9

**Table IV. Partition Coefficients Calculated for Different Solute Elements in the Cast Alloys Compared to Other Values Measured from Literature**

Alloy	Description	$k$ Ni	$k$ Cu	$k$ Fe	$k$ Mn	$k$ Si	$k$ Nb	$k$ V
1	high Si, low Nb	1.01	0.99	1.20	0.78	0.83	—	—
2	med. Si, low Nb	1.02	0.97	1.19	0.79	0.79	—	—
3	low Si, low Nb	1.03	0.93	1.11	0.89	0.89	1.30	—
4	med. Si, med. Nb	1.03	0.94	1.23	0.80	0.79	—	—
5	high Si, high Nb	1.03	0.95	1.29	0.74	0.82	0.96	—
6	low Si, high Nb	1.05	0.90	1.14	0.87	0.90	1.20	—
7	med. Si, high Nb	1.03	0.95	1.25	0.80	0.79	1.02	—
8	highest Cu, med. Si	1.10	0.95	1.21	0.93	1.02	—	—
9	high Cu, med. Si	1.04	0.96	1.21	0.80	0.82	—	—
10	V, med. Si	1.03	0.95	1.20	0.81	0.82	—	1.33
11	high Mn	1.02	0.97	1.26	0.95	0.85	—	—
Monel 400 <sup>[26]</sup>	—	1.08	0.78	—	—	—	—	—
Nb Bearing SA <sup>[27]</sup>	—	1.02	—	1.00	—	0.76	0.45	—
HR-160 <sup>[29]</sup>	—	0.96	—	—	—	0.71	—	—
In. 909 <sup>[28]</sup>	—	0.97	—	1.10	—	0.67	0.49	—

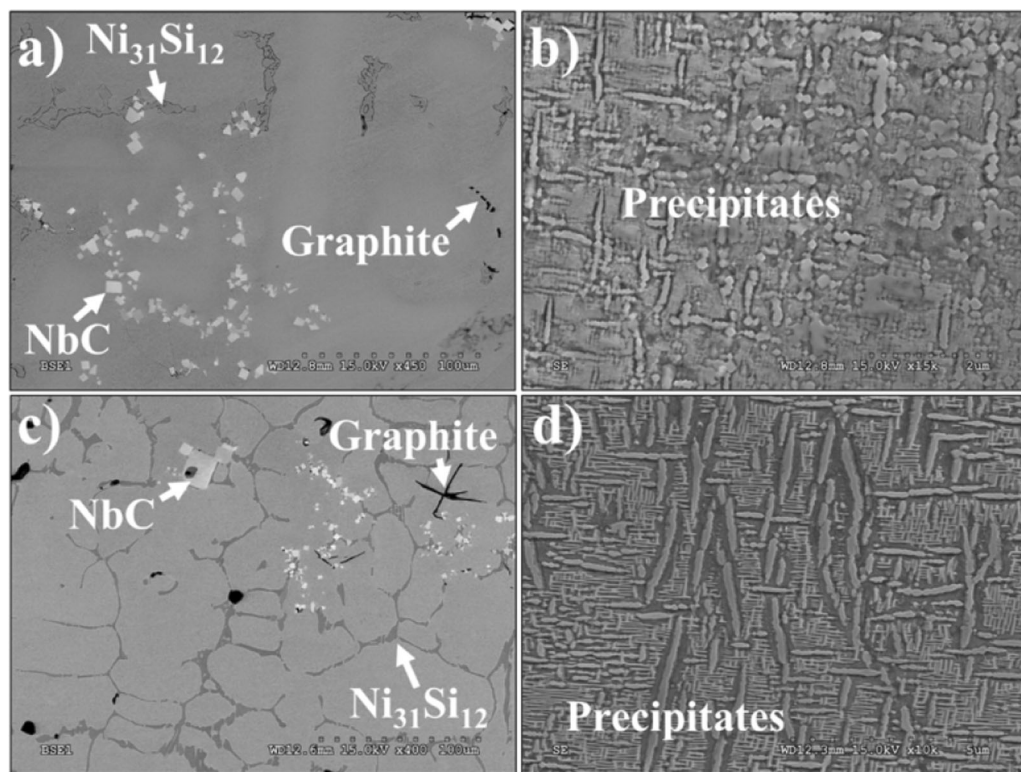


Fig. 5—SEM micrographs showing the microstructure of (a, b) Alloy 9 containing 45 wt pct Cu and 3 wt pct Si, and (c, d) Alloy 8 containing 60 wt pct Cu and 3 wt pct Si at low and high magnifications.

terminated at lower  $f_s$  value in accordance with the higher measured eutectic fraction. The profile also reached a lower average Si concentration in the interdendritic region, indicating a decrease in the maximum solid solubility limit as a result of the higher Cu concentration. This effect has been noted anecdotally in past reports, but has not been characterized or quantified experimentally in any prior work.<sup>[3,37]</sup> The reduction in the Si solubility limit from 4.76 wt pct measured in Alloy 4 (or 4.99 wt pct averaged from Alloys 1, 2, 4, 5, and 7) to 3.56 wt pct in Alloy 9,

explains the observed differences in the measured eutectic fraction. While the nominal Si concentration and segregation behavior between the alloys were similar, the reduction in the amount of Si that could remain in solid solution within the matrix caused the  $\gamma/\text{Ni}_{31}\text{Si}_{12}$  eutectic reaction to occur earlier on in the solidification path to accommodate the remaining solute.

The Si concentration in Alloy 8 (with 60 wt pct Cu) appeared to remain relatively constant around 2 wt pct Si and contained significant scatter within the data. The



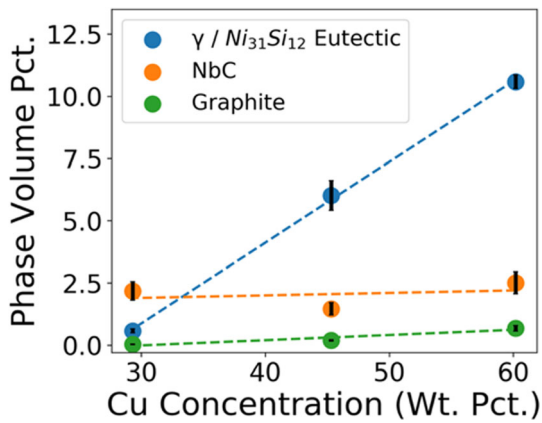


Fig. 6—The relationships between Cu concentration and the phase volume percents measured in the microstructures of Alloys 4, 8, and 9. Error bars represent the standard error from image analysis measurements.

high degree of noise was caused by the extensive solid-state precipitation that occurred during cooling from casting, and obscured much of the true Si segregation behavior which prevented accurate characterization of the solute profile. The measured  $k^{Si}$  value of 1.02 suggested that Si partitioned slightly to the dendrite core which was at odds with the high fraction of  $\gamma/Ni_{31}Si_{12}$  constituents in the interdendritic regions and thus did not describe the true segregation behavior in this heat. The increase in the eutectic volume fraction compared to Alloys 4 and 9 was consistent with a further reduction in Si solubility in the matrix phase, and/or a significant reduction in  $k^{Si}$ .

### C. Effect of V and Mn on Cast Microstructure and Solidification Path

Alloy 10 also contained a near equivalent composition to Alloy 4, but had the addition of 0.5 wt pct V. While V is not included in the ASTM A494 specification, it has been shown to reduce the formation of detrimental Si-rich intermetallic phases during the solidification of other Ni-base alloys, and to enhance the Ni–Si precipitation hardening behavior in several Cu–Ni–Si alloys.<sup>[38–41]</sup> The V addition did not significantly alter the cast microstructure compared to Alloy 4. Imaging in the SEM revealed NbC particles, intermetallic eutectic constituents identified as  $Ni_{31}Si_{12}$  via EPMA measurements, and Ni–Si precipitates in similar quantities to Alloy 4. While not present in sufficient quantities to identify through XRD, the precipitates were assumed to be  $\beta_1$  due to the similarities in size, shape, and morphology compared to the Si–Nb varying alloys. The only discernable difference in microstructure between Alloys 10 and 4 was the absence of graphite which was observed in small amounts  $< 0.1$  vol pct in Alloy 4.

The DSC measured phase transition temperatures for Alloy 10 are listed in Table III. The addition of V did not significantly influence  $T_L$ ; however, the measured eutectic temperature of 1026 °C was less than that measured in Alloy 2. A reduction in  $T_e$  was also

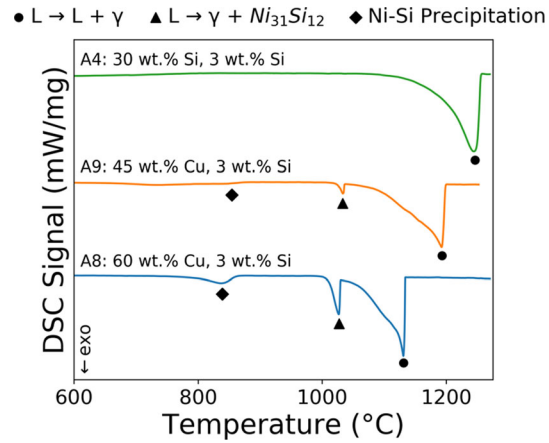


Fig. 7—On-cooling DSC data for Alloys 4, 8, and 9 containing variations Cu concentration. Relevant phase transformation peaks are marked with indicators.

observed in a prior work by Mo *et al.* which noted that the addition of V appeared to slightly reduce the terminal Laves phase reaction temperature in Inconel 718.<sup>[38]</sup> The STR of Alloy 10 was estimated to be 236 °C which was the highest among the investigated alloys.

Table IV lists the measured partition coefficients in Alloy 10. The segregation behavior of each element was in excellent agreement with prior measurements from Alloy 4, showing that the addition of V had no measureable effect on solute partitioning. The high measured  $k^V$  of 1.33 indicated substantial segregation of V to the solid phase during the solidification process. No appreciable solubility of V was measured in any of the eutectic constituents or carbide phases, and the maximum solid solubility limit of Si in the matrix remained unchanged.

The composition of Alloy 11 was also analogous to Alloy 4, but with an increase in Mn concentration from ~ 1.5 to 10 wt pct. The cast microstructure of Alloy 11 is shown in Figure 9. It was found to have nearly equivalent volume fractions of primary NbC and graphite to Alloy 4, but contained a markedly different intermetallic phase within the eutectic constituents. EPMA measurements taken from the intermetallic are listed in Table II. The chemical composition of the phase and location of two small peaks in the XRD diffractogram shown in Figure 2(b) were consistent with a Mn-enriched G phase with a stoichiometry similar to the Nb-enriched G phase observed in Alloy 5. Despite the fixed Si concentration of 3 wt pct, the fraction eutectic increased to 7.8 vol pct in Alloy 11, showing that Mn concentration had a significant role in intermetallic formation. Additional microstructural characterization revealed that a mix of cubic and elongated precipitates formed in the cast microstructure, primarily in the interdendritic regions. The precipitates were assumed to be  $\beta_1$ , but the identity could not be confirmed due to the lack of representative peaks corresponding to  $\beta_1$  or other silicide phases in the XRD data. Similar formation of G phase and  $Ni_3Si$  has been observed in the as-solidified microstructure of other Ni–Mn–Si–Cu alloys.<sup>[42]</sup>

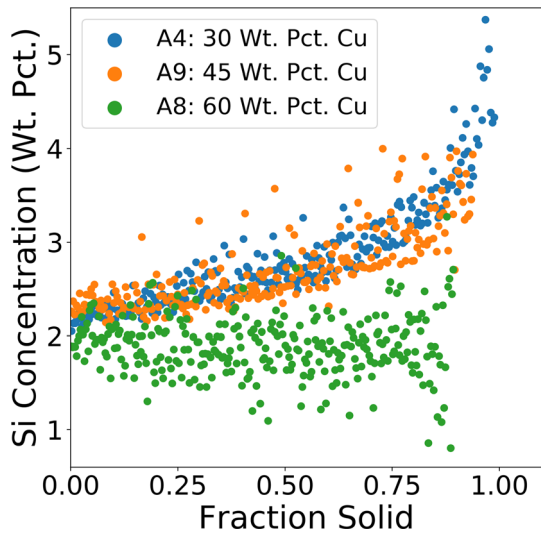


Fig. 8—Si solid concentration profiles Figure in Alloys 4, 8, and 9 measured using EPMA and sorted using the WIRS scheme.

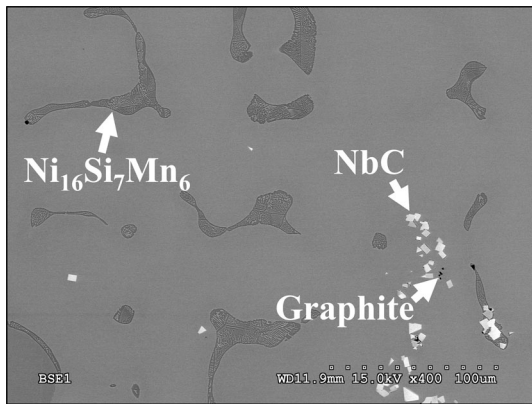


Fig. 9—SEM image showing the microstructure of Alloy 11 containing 10 wt pct Mn and 3 wt pct Si.

Table III shows that the increase in Mn concentration also significantly reduced  $T_L$  and  $T_e$  compared to those measured in Alloy 4. The liquidus temperature was reduced from 1265 °C to 1174 °C, while the  $\gamma/G$  Phase eutectic reaction was measured to start at 989 °C which was the lowest  $T_e$  measured among the Monel alloys in this work. This resulted in an estimated STR of 185 °C which was relatively low compared to the other alloys.

Characterization of solute partitioning in Alloy 11 revealed that despite the changes to the microstructure, the Mn concentration did not significantly alter segregation in the Monel system. The measured partition coefficients for Alloy 11 listed in Table IV were in close agreement with those from Alloy 4. Similar to previous results, the increase in Mn concentration also reduced the measured maximum solid solubility limit of Si in austenite down to 3.15 wt pct, which was lower than measurements from Alloys 4 and 9. These data confirmed reports by Lashko *et al.* who speculated that Mn may have a similar influence to Cu on the extent of Si

solubility in austenite within Monel alloys.<sup>[37]</sup> The reduction in solubility limit paired with the segregation of Si in Alloy 11 resulted in the high eutectic fraction that was greater than that measured in Alloys 4 and 9.

#### D. Effects of Composition on Tensile Properties

Table V lists the results of hardness and tensile testing performed on the cast alloys showing that they spanned a wide range of mechanical properties based on composition. Figure 10 shows histograms of the hardness measurements for several alloys showing the dispersion of hardness throughout the microstructures of the castings. The low indent load and small indenter tip size resulted in indents that were smaller than the dendrite arm spacing of the alloys, and thus individual hardness measurements reflected the localized hardness of the respective regions of the microstructure. Alloys that did not contain any precipitates, such as the ~ 1 wt pct Si heat in Figure 10(a), exhibited narrow distributions of hardness due to the general homogeneity of the microstructure. The hardness of the austenitic matrix was largely constant, and the presence of small graphite and carbide particles had minimal influence on the measurements. As Si concentration was increased up to 3 wt pct, a much broader distribution of hardness was measured due to the gradients in  $\beta_1$  precipitation between the dendrite cores and interdendritic regions. Indents located within the precipitate-denuded dendrite core areas had lower measured hardness values, while indents located in precipitate-rich interdendritic regions had correspondingly increased resistance to indentation. With further increases in Si concentration up to 4.4 wt pct, precipitates were observed to cover a much larger portion of the overall microstructure, and thus exhibited a tighter spread of hardness that was shifted to higher values.

Similar behavior was observed for the effects of Cu concentration shown in Figure 10(b). The 30 wt pct Cu sample (Alloy 4) was observed to have a broad hardness profile, similar to that of Alloy 2 from Figure 10(a), due to the large precipitate gradients. Increases in Cu content up to 45 wt pct were previously shown to reduce the Si solubility limit, promote precipitation throughout all regions of the microstructure, and produce higher fractions of  $Ni_{31}Si_{12}$  intermetallic constituents. These changes reduced the variations between different regions of the microstructure and increased the average hardness. Further increase in Cu content to 60 wt pct were observed to significantly alter the morphology of the precipitates from spherical or cubic, to needle-like. The large reduction in hardness measured in Alloy 8 suggests that this change to the precipitation behavior considerably reduced the strengthening effects compared to those observed in Alloy 9.

Figure 11 plots the tensile yield strength and UTS of the Monel alloys as a function of average hardness. While hardness (HV) was shown to correlate with both strength metrics, a much stronger linear relationship with yield strength (YS) was observed and is described by Eq. [4].

**Table V. Hardness and Tensile Properties of the Cast Monel Alloys Compared to the Minimum Requirements from the ASTM A494 Specification<sup>[1]</sup>**

Alloy	Description	Avg. Hardness (HV)	Yield Strength (MPa)	UTS (MPa)	Pct. Elongation
1	high Si, low Nb	433 ± 39	931 ± 41	951 ± 62	0.7 ± 0.3
2	med. Si, low Nb	325 ± 61	638 ± 14	831 ± 24	7.0 ± 0.0
3	low Si, low Nb	160 ± 8	210 ± 0	522 ± 5	37.5 ± 2.5
4	med. Si, med. Nb	312 ± 65	624 ± 34	852 ± 38	14.5 ± 2.5
5	high Si, high Nb	447 ± 52	876 ± 0	876 ± 0	1.5 ± 0.3
6	low Si, high Nb	149 ± 14	197 ± 5	486 ± 3	27.0 ± 3.0
7	med. Si, high Nb	345 ± 53	612 ± 16	858 ± 3	10.5 ± 0.5
8	highest Cu, med. Si	297 ± 44	483 ± 27	483 ± 27	1.2 ± 0.8
9	high Cu, med. Si	410 ± 26	955 ± 3	996 ± 3	2.1 ± 0.1
10	V, med. Si	349 ± 57	700 ± 10	896 ± 34	10.0 ± 2.0
11	high Mn	388 ± 46	776 ± 17	776 ± 17	0.8 ± 0.1
Minimum Tensile Requirements Per ASTM A494					
M35-1	low Si	—	170	450	25
M30C	low Si	—	225	450	25
M30H	med. Si	—	415	690	10

Measured tensile values represent the average of two tests.

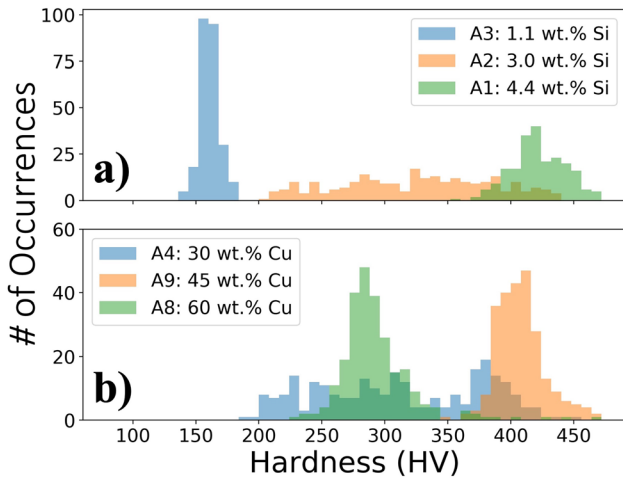


Fig. 10—Histograms showing effects of (a) Si concentration in Alloys 1, 2, and 3, and (b) Cu concentration in Alloys 4, 8, and 9 on the distributions of hardness measured across the cast microstructures.

$$YS = 2.56HV - 204.85, \quad r^2 = 0.96. \quad [4]$$

The tensile results from Alloys 1–7 are plotted in Figure 12 and show the effects of Si and Nb concentration on the yield strength, UTS, and ductility of the cast samples. Yield strength was shown to scale linearly with Si concentration between 1 and 4.4 wt pct in accordance with Eq. [5].

$$YS = 210.5C^{Si} - 11.7, \quad r^2 > 0.99. \quad [5]$$

The negative  $y$ -intercept of Eq. [5] shows that the true relationship is sigmoidal over a wider range of Si

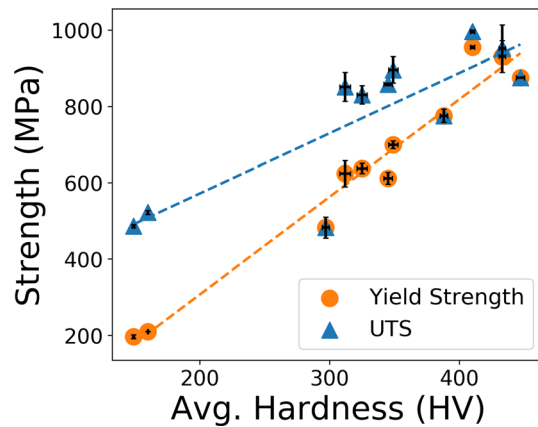


Fig. 11—The tensile yield strength and UTS plotted as a function of average hardness showing positive correlations.

contents rather than linear which was consistent with the findings of a prior tensile study by Eash and Kihlgren.<sup>[3]</sup> Microstructural characterization has suggested that the improvements to strength in the 3 and 4.4 wt pct Si alloys resulted from the increase in  $\beta_1$  precipitation strengthening. Since the low-Si heats exhibited negligible precipitation, further reductions in Si would be expected to have a marginal impact on strengthening. Figure 12(a) also shows that Nb concentration and the associated changes in NbC and graphite fractions within the microstructure did not have a discernible effect on yield strength across the range of Si levels.

Ultimate tensile strength was shown to scale with Si concentration as shown in Figure 12(b), but the improvements tapered off at higher Si levels due to the reductions in ductility and associated lack of strain hardening. The ductility was plotted in Figure 12(c) and was shown to decrease significantly with increasing Si

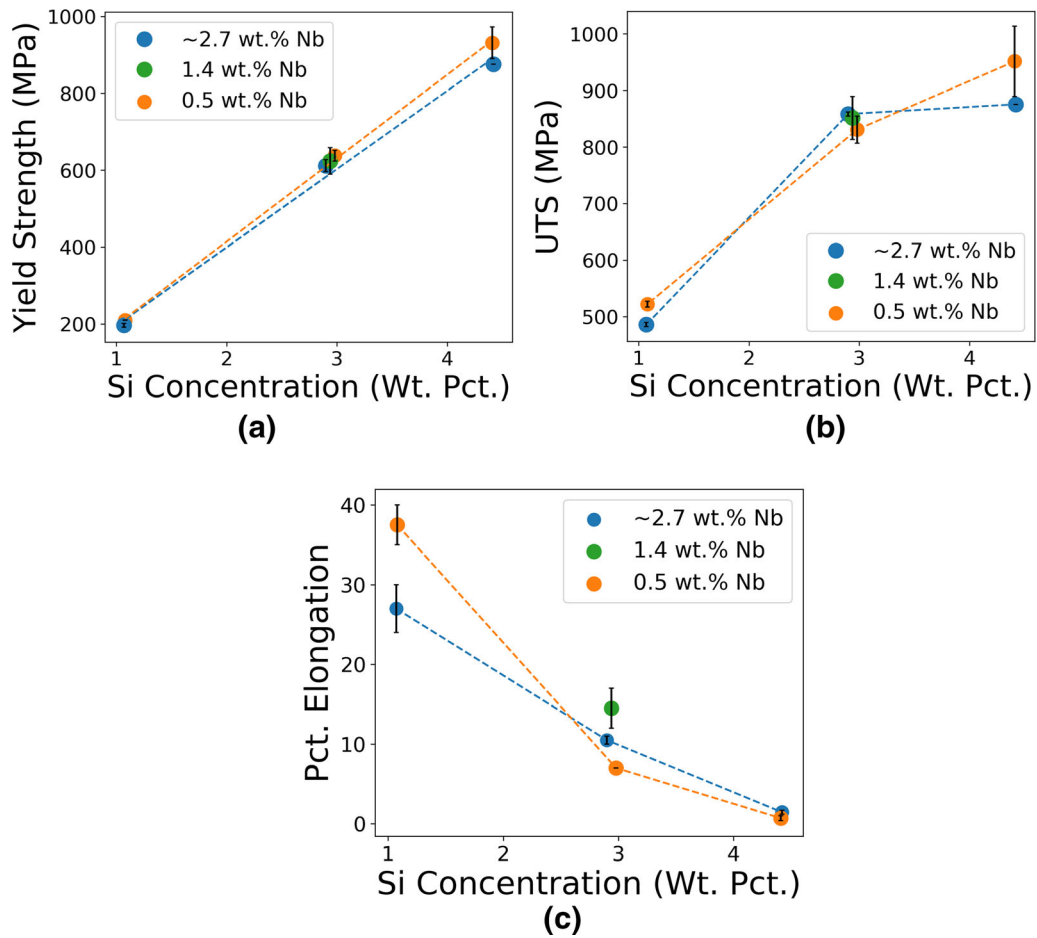


Fig. 12—The effects of Si and Nb concentration on the (a) yield strength, (b) UTS, and (c) percent elongation of cast Monel Alloys 1–7.

concentration, reaching elongations of less than one percent at the highest Si levels indicating minimal plastic deformation before failure. No clear trends between Nb concentration and ductility were found in the medium or high-Si grades, but a substantial reduction in elongation with increasing Nb concentration was observed between the two low-Si grades. Alloys 3, 4, 6, and 7 met the respective minimum requirements of grades M35-1 or M30H for yield strength, UTS, and elongation defined in the ASTM A494 specification.<sup>[1]</sup> Alloy 2 did not meet the minimum requirements due to the low ductility.

Figure 13 plots the yield strength, UTS, and elongation from Alloys 4, 9, and 8. As Cu concentration increased from 30 to 45 wt pct, yield strength increased significantly from 624 to 955 MPa, which was the highest among all tested alloys. The ultimate tensile strength was also higher in Alloy 9, but by a smaller amount attributable to the drop in ductility and strain hardening. The enhanced mechanical properties in Alloy 9 were consistent with the reduction in Si solubility, and subsequent increase in silicide precipitation. The additional increase in Cu concentration up to 60 wt pct was highly detrimental to properties. Both yield strength and UTS were reduced compared to Alloys 4 and 9, in accordance with the lower measured hardness and elongation. These reductions in mechanical properties

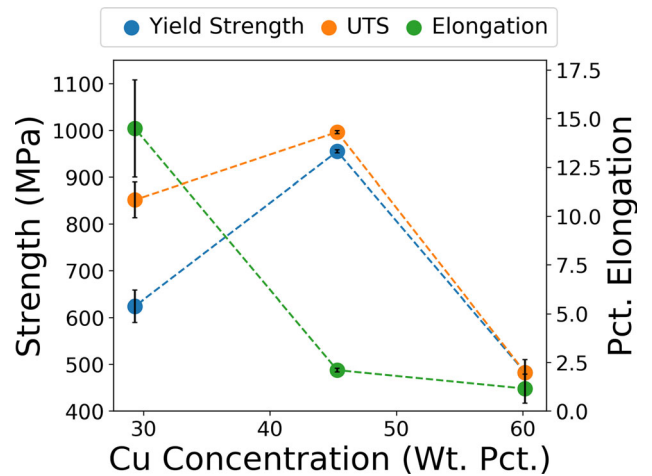


Fig. 13—The effect of Cu concentration on the yield strength, UTS, and percent elongation of cast, 3 wt pct Si Monel alloys.

were likely related to the observed changes in precipitation. Additional work using TEM would be necessary to fully understand the mechanisms of softening. Alloys 8 and 9 did not meet the minimum elongation requirement of 10 pct for M30H, and Alloy 8 also did not reach the minimum UTS of 690 MPa.<sup>[1]</sup>



The results in Table V show that the addition of 0.5 wt pct V improved the yield strength and UTS in Alloy 10 compared to Alloy 4. Due to the lack of detectable differences in microstructure between the two alloys, the strengthening mechanism caused by the V addition was not immediately clear. Vanadium has been previously shown to be an effective solid solution strengthening element in the austenitic matrix of Ni-base alloys and in  $Ni_3X-L1_2$  phases.<sup>[43,44]</sup> Prior research has also shown that V is readily soluble in  $\beta_1$  up to 6 at. pct by substituting for Si atoms and can thus provide appreciable strengthening to the precipitates.<sup>[45]</sup> Despite the effects on strength, the addition of V slightly reduced the ductility. All minimum tensile properties defined in the ASTM requirement for M30H were still met.

The tensile results for Alloy 11 showed that the higher Mn concentration also led to an increase in yield strength, likely relating to the reduction in the Si solubility limit and promotion of silicide precipitation. Manganese is also a known solid solution strengthener in austenite and  $L1_2$  precipitates and has been shown to be soluble in  $\beta_1$  up to 7.8 at. pct.<sup>[45]</sup> Both yield strength and UTS were sufficient to meet the minimum requirements. However, the sharp reduction in elongation down to 0.8 pct was well below the minimum requirement for M30H.<sup>[1]</sup>

To understand how composition and the associated changes to microstructure related to the observed variations in tensile ductility, SEM imaging of the fracture surfaces and subsurface secondary cracking in the tensile samples was performed. Figure 14 shows

representative images of two grades that exhibited ductile and brittle tensile failures. The fracture surfaces of Alloys 2, 3, 4, 6, 7, and 10 consisted primarily of microvoid coalescence (MVC), typical of samples that underwent extensive plastic deformation, which correlated with the relatively high elongations of at least seven percent. Alloy 2 did exhibit some regions of quasi-cleavage within the fracture surface. In some samples, groupings of faceted NbC particles were observed on the ductile fracture surfaces. Figure 14(b) shows a representative image of subsurface secondary cracking in the low-Si Monel grades. Shear bands were observed throughout the matrix indicative of plastic deformation, and extensive cracking through groupings of primary carbides was also observed. Cracking through elongated script carbides occurred in Alloys 2 and 3, which contained low-Nb concentrations, particularly for carbides oriented perpendicular to the loading direction.

The subsurface cracking paired with the observation of carbide groupings that lined the fracture surfaces indicated that these phases were contributing to failure and the measured discrepancy in elongation between the low-Si alloys. Alloy 6 contained more Nb and a higher volume fraction of primary carbides that agglomerated into large groups during solidification. This resulted in a higher number of crack nucleation sites, longer paths for brittle crack propagation, and more significant stress concentration within the matrix compared to the lower-Nb alloy. No cracking was observed through graphite particles in any of the low-Nb alloys, although detection

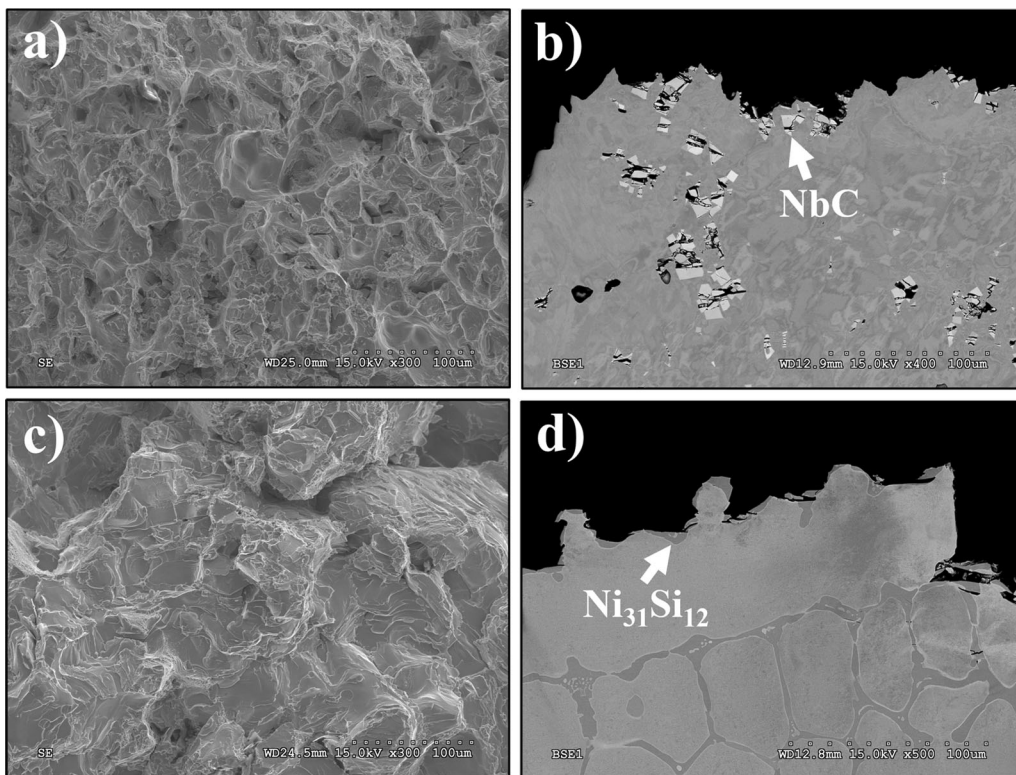


Fig. 14—SEM images showing representative fracture surfaces and subsurface secondary cracking in (a, b) Alloy 6 and (c, d) Alloy 8.

of damage within these phases was difficult due to the low brightness of graphite when imaged in the SEM. In Alloys 2, 4, 7, and 10, subsurface cracking was also observed through  $\gamma/\text{Ni}_{31}\text{Si}_{12}$  eutectic constituents in addition to NbC. No clear trends were observed between Nb concentration or NbC volume fraction and ductility in those heats, suggesting that carbide cracking had less influence over the ductility when the intermetallic eutectic constituents were present. The reduced effects of carbides on tensile ductility in heats that formed Si-enriched intermetallics has been noted in other Ni-base alloys as well.<sup>[46]</sup>

The fracture surfaces of Alloys 1, 5, 8, 9, and 11 contained predominately quasi-cleavage failure as is shown in Figure 14(c) which was consistent with the low measured elongations. The fracture surfaces also appeared dendritic in nature, as failure occurred preferentially through the interdendritic regions of the microstructure. Small, localized areas of MVC were observed and were believed to have occurred in areas near the dendrite core that were locally soft due to the absence of silicides. Secondary cracks in these alloys were found almost exclusively through  $\gamma/\text{silicide}$  eutectic constituents, with minimal to no cracking found through NbC particles. In general, secondary cracking was only observed in very close proximity to the fracture surface as is shown in Figure 14(d), where failure occurred through a continuous network of  $\text{Ni}_{31}\text{Si}_{12}$ . Silicides further below the surface remained undamaged. Each of the brittle heats contained high fractions of eutectic constituents that formed as connected networks rather than in discrete pockets as was observed in Alloys 2, 4, and 7. These images revealed that cracks likely nucleated within intermetallic constituents at lower stresses than in NbC particles, and that failure occurred primarily by brittle crack propagation through intermetallics in the interdendritic regions resulting in quasi-cleavage failure.

The detrimental effects of eutectic formation on the ductility and transition in failure mode is made clear by the plot in Figure 15 where percent elongation is plotted as a function of fraction eutectic. Outside of the two low-Si grades, where differences in ductility were explained by differences in carbide fraction and morphology, elongations were shown to decay exponentially with the fraction of eutectic. This trend occurred for the alloys with increasing Si concentration, as well as for grades with higher Cu and Mn concentration that increased eutectic fraction at a fixed Si content. The findings were in good agreement with a prior study by Wang *et al.* in which a transition from MVC to quasi-cleavage failure was also observed in Ni-Cu-Si alloys with increasing Si content.<sup>[4]</sup>

### E. Effect of Composition on Solidification Cracking Susceptibility

Figure 16 shows the FZ microstructures of Alloys 4 and 8 taken from welded sections of the Varestraint samples. The FZ microstructures contain NbC and Si-rich intermetallic eutectic constituents in the interdendritic regions and are shown to be very similar to the

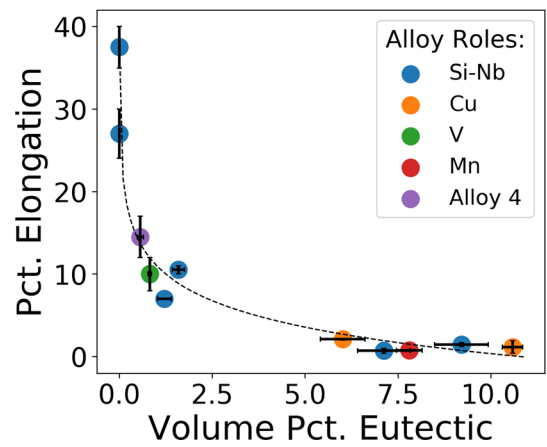


Fig. 15—Percent elongation as a function of the measured volume percent Ni-Si eutectic constituents. Error bars for the eutectic percents represent the standard errors from image analysis measurements.

cast microstructures from Figures 1 and 5. Nanoscale precipitates were also still present throughout the interdendritic regions despite the rapid cooling conditions imparted during the welding process. Consistency between cast and welded microstructures was observed for all of the Monel heats in this work. The only detectable differences were a higher propensity for secondary NbC formation in place of primary NbC observed in Alloys 1, 4, 5, 7, and 10. Prior work on similar Ni-base alloys has shown that a change in carbide reaction sequence can be induced by increases in the solidification rate that leaves less time for primary MC particles to nucleate and grow from the melt.<sup>[47,48]</sup> This change in morphology was observed in the FZ due to the rapid cooling conditions during welding.

The results of the Varestraint testing performed on the alloys with systematic variations in Si and Nb (Alloys 1–7) are plotted in Figure 17. The MCL in the FZ induced during testing was used as the metric to quantify solidification cracking susceptibility and is shown to scale with increasing Si concentration. Alloys 3 and 6, containing 1 wt pct Si, exhibited relatively low susceptibility to cracking, with MCL values only slightly larger than those in wrought 304L stainless steel, which is known to have very good resistance to solidification cracking.<sup>[23]</sup> This is consistent with the results of Varestraint testing in prior works that have shown that low-Si Monels like M35-1, Monel 400, and M30C generally have good weldability.<sup>[7,8]</sup> As Si concentration was increased to 3 wt pct, the weldability was sharply reduced as MCL measurements exceeded 6 mm. Raising Si concentration to 4.4 wt pct resulted in minimal further increases to MCL as the cracks were constrained by the boundaries of the FZ. This is displayed in the inlaid stereomicrograph in Figure 17, which shows that the solidification cracks propagating out from the weld center line extended the entire width of the FZ. The abrupt increase in MCL with increasing Si concentration notably coincided with the onset of the terminal  $L \rightarrow \gamma + \text{Ni}_{31}\text{Si}_{12}$  eutectic reaction at the end of solidification. Weldability was generally observed to be

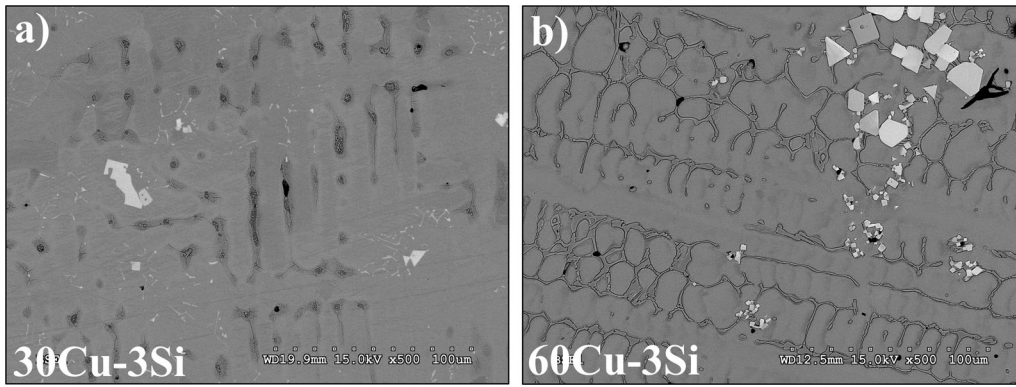


Fig. 16—Example fusion zone micrographs taken from (a) Alloy 4 and (b) Alloy 8, showing similar microstructures to the cast samples.

independent of Nb concentration. A slight decrease in MCL was observed in Alloy 6 relative to Alloy 3 among the low-Si grades, but no statistically significant effect was observed among the other five alloys that had higher Si contents.

To confirm the mode of cracking and investigate the mechanisms behind the observed changes in cracking susceptibility with composition, metallography was performed on cracked sections of the Varestraint bars and images from Alloy 5 are presented in Figure 18. The crack faces exhibited dendritic morphologies that were characteristic of solidification cracking through partially solidified dendrites. Imaging of the crack tips in Figure 18(b) revealed that they propagated through interdendritic areas that contained solute enriched liquid that later solidified as  $\gamma/\text{Ni}_{31}\text{Si}_{12}$  eutectic. Imaging on Alloys 8–10 showed similar results, indicating that low temperature eutectic reactions during solidification contributed to the solidification cracking susceptibility. In the low-Si alloys that did not form any eutectic during solidification, cracking was observed along grain boundaries.

The Varestraint results for all of the Monel alloys are shown aggregated in Figure 19 and are plotted as a function of measured volume percent eutectic. Results for Alloy 11 are not shown, as the low base metal ductility could not accommodate the applied bending strain and prevented testing of that alloy. This plot clearly shows that all alloys that formed Si-rich intermetallic eutectic constituents had comparably high susceptibilities to solidification cracking. Changes to Cu and V concentrations had minimal effects on MCL. The measured crack lengths in the eutectic-bearing heats were very high compared to measurements from other Ni-base alloys tested under the same conditions.<sup>[49]</sup>

It has been well established that solidification cracking occurs in the final stages of solidification when tensile stresses (induced by thermal contraction and solidification shrinkage) are applied across the mushy zone, and the networks of impinging dendrites inhibit fluid flow to strained areas to fill the expanding volume. For the case of cast Monel alloys containing at least 3 wt pct Si, the results of this work indicate that the segregation of Si stabilized small quantities of residual liquid down to relatively low temperatures and delayed

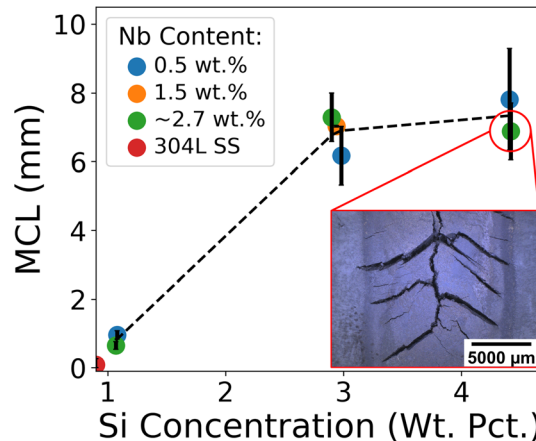


Fig. 17—Results of Varestraint testing performed on Alloys 1–7 showing the relationship between MCL and Si concentration. The inlaid image shows a stereomicrograph of the surface cracking in an Alloy 5 Varestraint sample.

dendrite coalescence. These effects likely left the structure weakened and unable to resist the tensile stresses that evolved during solidification. To confirm this mechanism of cracking, the liquid fraction ( $f_L$ ) as a function of temperature for several example alloys with varying Si concentrations were calculated and are plotted in Figure 20. CALPHAD software packages such as Thermo-Calc were previously found to be ineffective at performing solidification simulations on Si-bearing cast Monel alloys using the available thermodynamic databases.<sup>[19]</sup> The plots were instead computed using the differential mass balance form of the Scheil non-equilibrium solidification equation, given by Eq. [6], and data from a Monel alloy pseudo-binary solidification diagram. The creation of the solidification diagram and the Scheil-type calculation procedure have been explained in detail in prior work.<sup>[19]</sup>

$$df_s = \frac{1 - f_s}{C_L - C_s} dC_L. \quad [6]$$

Equation 6 was used to compute  $C_L$  as a function of  $f_s/f_L$ , which was then related to temperature through the equation of the liquidus line given in the solidification



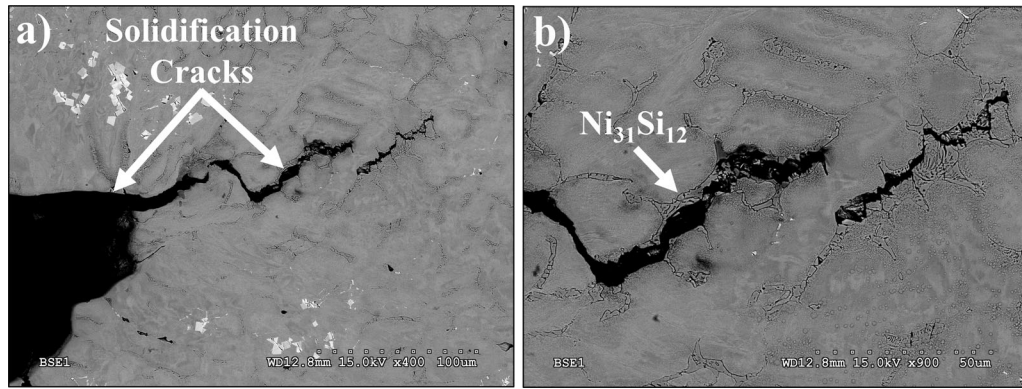


Fig. 18—Fractography performed on a Varestraint sample of Alloy 5 at (a) low magnification, and (b) higher magnification, showing solidification cracks propagating through intermetallic eutectic constituents.

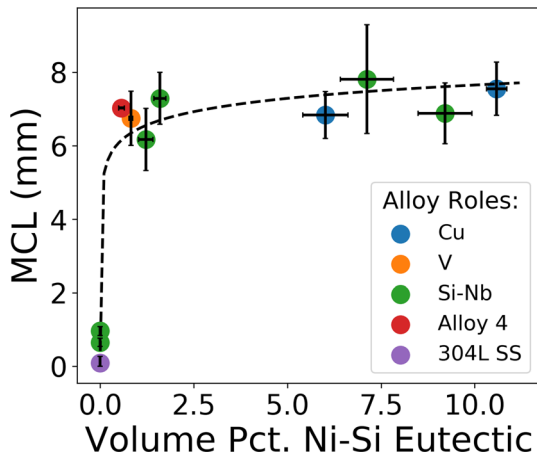


Fig. 19—Results of Varestraint testing showing the relationship between the MCL and the volume percent of Ni-Si eutectic constituents. Data for 304L stainless steel are plotted for reference. Error bars for the eutectic percents represent the standard errors from image analysis measurements.

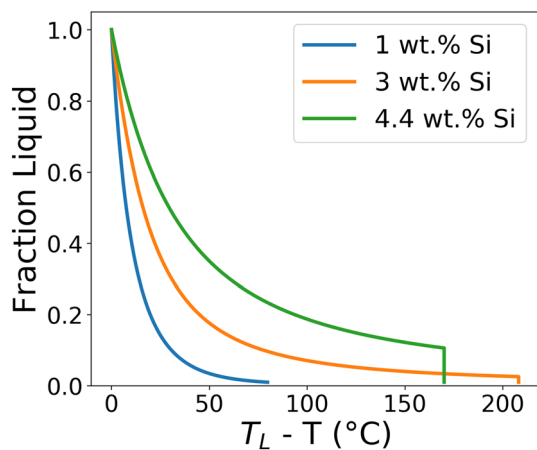


Fig. 20—Fraction liquid vs temperature plots (normalized by liquidus temperature) for alloys with varying Si content calculated using the Monel alloy solidification diagram. The calculations were terminated at  $f_L = 0.01$ .

diagram. The diagram was constructed using data from Alloys 1–7 and was thus not representative of the solidification behavior of Alloys 8–11.

Figure 20 shows that the variation in fraction liquid with temperature within the mushy zone of the 1 wt pct Si alloy did not reach the eutectic point, completed solidification over a short temperature interval, and thus exhibited correspondingly low susceptibility to cracking during Varestraint testing. The plots for the medium and high-Si alloys showed that Si segregation significantly increased the effective solidification temperature ranges of the alloys. The fraction liquid profiles also exhibited shallow slopes at high- $f_s$  intervals, indicating that the presence of residual liquid films between encroaching dendrites was insensitive to temperature, and thus likely to promote cracking by inhibiting coalescence. These observations were consistent with the proposed mechanisms of cracking.

Prior work by Kou developed a solidification cracking model based around these concepts, and defined a cracking susceptibility coefficient (CSC), given by Eq. [7], by which to rank alloys.<sup>[50]</sup>

$$\text{Kou CSC} = \left| \frac{dT}{d(f_s^2)} \right|_{T_c} \frac{T_{\text{coh}}}{T_c} \quad [7]$$

This equation represents the average slope of a modified temperature vs  $f_s$  profile over a specified temperature interval near the end of solidification. The coherency point ( $T_{\text{coh}}$ ) is the temperature at which dendrites in the mushy zone begin to grow into one another, restricting pathways for fluid to flow, and the coalescence point ( $T_c$ ) is the temperature at which neighboring dendrites have sufficiently conjoined to act as a cohesive solid. The coherency and coalescence temperatures (and corresponding fraction solid values) are widely acknowledged to be system dependent and can change significantly based on solute content.<sup>[50,51]</sup> Using the Scheil analysis and solidification diagram data, the Kou CSC was calculated as a function of nominal Si concentration to forecast the solidification cracking susceptibility of the Monel system over a range



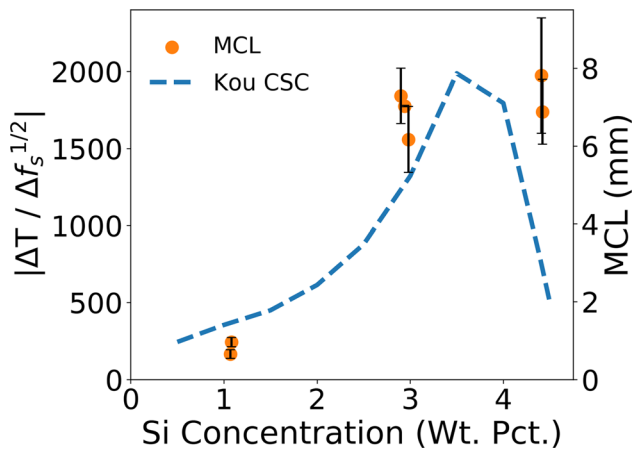


Fig. 21—The calculated Kou CSC plotted as a function of nominal Si concentration showing reasonable agreement to the maximum crack lengths measured after Varestraint testing of Alloys 1–7.

of compositions. The CSC values were computed over the  $f_s$  interval of 0.87 to 0.94 in accordance with Kou's calculation procedure from previous work.<sup>[50]</sup>

The results are plotted in Figure 21 alongside the Varestraint results from Alloys 1–7. At low Si concentrations, the CSC calculations predict very low susceptibility to cracking, which was consistent with the small MCL values measured in the Varestraint samples of Alloys 3 and 6. As Si concentration was increased to 3 wt pct, the Kou CSC predicted a substantial increase in cracking susceptibility that generally agreed with the MCL measurements from Alloys 2, 4, and 7, and the extension of the STR predicted by the  $f_L$  plots. Further increases in Si content beyond 3.75 wt pct were predicted to reduce cracking susceptibility, as the Kou CSC curve took the characteristic 'Λ'-shape that has been reported in previous works that related composition to solidification cracking susceptibility.<sup>[52,53]</sup> The reduction in predicted susceptibility at high solute contents was attributed to the greater ease in liquid feeding when the amount of solute enriched liquid is sufficiently high. Despite the predicted improvement in weldability, the large MCL measurements in the high-Si Alloys indicated worsening cracking susceptibility and insufficient feeding of liquid to backfill the solidification cracks.

The differences between the observed and modeled behavior may relate to changes in the coherency point caused by the variations in composition. By manually adjusting the coherency temperatures used in the CSC calculations as a function of Si content, the peak of the Λ-curve could be shifted to higher concentrations which better agreed with the Varestraint data. The solidification diagram was also previously shown to slightly overpredict the fraction eutectic, and thus fraction of residual liquid near the end of solidification, at medium to high Si levels. This may have also contributed to the disagreement with the modeled cracking susceptibilities.

Additional testing on alloys with Si concentrations greater than 4.4 wt pct would be necessary to determine if/when crack healing by liquid feeding would become significant during the welding of Monel alloys.

#### IV. CONCLUSIONS

In this study, the effects of broad variations in composition on the solidification behavior, microstructure, tensile properties, and solidification cracking susceptibility of cast Monel alloys were assessed. The following conclusions can be drawn as a result of this work.

1. Si segregation to the liquid during solidification led to  $\gamma$ /silicide eutectic reactions in alloys containing at least 3 wt pct Si.
2. Increasing Cu and Mn concentrations reduced the solubility limit of Si in austenite and promoted additional silicide formation in 3 wt pct Si Monels.
3. Increases in Si concentration from 1 to 4.4 wt pct and Cu concentration from 30 to 45 wt pct led to significant improvements in yield strength and UTS, but were highly detrimental to ductility.
4. Nb concentration did not have a discernible influence on strengthening.
5. Si-rich eutectic constituents reduced ductility by nucleating cracks and offering brittle paths for crack propagation during loading. Groupings of NbC particles had similar effects in low-Si grades that did not contain eutectic.
6. The terminal  $\gamma$ /silicide eutectic reactions severely increased susceptibility to solidification cracking by stabilizing residual liquid in the interdendritic regions down to relatively low temperatures. Low-Si grades that did not undergo eutectic reactions had generally low susceptibility to cracking.

#### ACKNOWLEDGMENTS

Sandia National Laboratories is a multi-mission laboratory managed and operated by National Technology and Engineering Solutions of Sandia, LLC, a wholly owned subsidiary of Honeywell International, Inc., for the US Department of Energy's National Nuclear Security Administration under Contract DE-NA0003525.

#### FUNDING

This research is sponsored by the DLA-Troop Support, Philadelphia, PA and the Defense Logistics Agency Information Operations, J68, Research & Development, Ft. Belvoir, VA.

## CONFLICT OF INTEREST

On behalf of all authors, the corresponding author states that there is no conflict of interest.

## REFERENCES

1. ASTM International: *ASTM A494*, ASTM International, West Conshohocken, 2019.
2. M. Sahoo, R.J. Lacroix, and P. Newcombe: *AFS Trans.*, 2002, vol. 92, pp. 239–51.
3. J.T. Eash and T.E. Kihlgren: *Trans. Am. Foundrymen's Soc.*, 1949, vol. 57, pp. 535–45.
4. S. Wang, J. Jie, B. Dong, S. Liu, T. Wang, and T. Li: *Mater. Sci. Technol. (UK)*, 2020, vol. 36, pp. 1671–84.
5. H. Vastenhold and T. Fukuda: *Proc. Asia Pac. Oil Gas Conf.*, 1993, pp. 221–28.
6. K. Devendranath Ramkumar, N. Arivazhagan, S. Narayanan, M. Narayanan, A. Mondody, and R. Kashyap: *Adv. Mater. Res.*, 2012, vol. 383–390, pp. 4693–96.
7. C.D. Lundin, R.A. Buchannan, C.C. Chen, I. Lee, and K.K. Khan: *SFSA Tech. Oper.*
8. A.C. Lingenfelter: *Weld. J. (Miami Fla)*, 1972, vol. 51, pp. 430–36.
9. C. Houska: *Castings: Stainless Steel and Nickel Base*, Nickel Institute, Durham, 2000.
10. W.M. Spear: *Nickel Base Casting Problems and Solutions*, SFSA Internal Report, Nickel Development Institute, pp. 1–9.
11. A.G. Evgenov, G.I. Morozova, and V.I. Lukin: *Met. Sci. Heat Treat.*, 2006, vol. 48, pp. 364–67.
12. J.N. Dupont, C.V. Robino, and A.R. Marder: *Weld. J.*, 1998, vol. 77, pp. 417–31.
13. J.N. DuPont, J.R. Michael, and B.D. Newbury: *Weld. J.*, 1999, vol. 78, p. 408-s.
14. I.S. Maroef, M.D. Rowe, and G.R. Edwards: *Hot Crack. Phenomenon Welds*, Springer, Berlin, 2005, pp. 119–40.
15. ASTM International: *ASTM E-407*, vol. 07, West Conshohocken, ASTM International, 2016, pp. 1–22.
16. M.D. Abrámoff, P.J. Magalhães, and S.J. Ram: *Biophotonics Int.*, 2004, vol. 11, pp. 36–41.
17. J.J. Donovan, D. Kremser, J.H. Fournelle, and K. Goemann: *Probe for EPMA Software: Acquisition, Automation, and Analysis*, Probe Software Inc., Eugene, 2012.
18. M. Ganesan, D. Dye, and P.D. Lee: *Metall. Mater. Trans. A*, 2005, vol. 36A, pp. 2191–2204.
19. C.J. Farnin, E.N. Coker, P.A. Salinas, and J.N. Dupont: *Metall. Mater. Trans. A*, 2023, vol. 54A, pp. 4716–30.
20. ASTM International: *American Society for Testing and Materials Handbook*, West Conshohocken, ASTM International, 2017, pp. 281–93.
21. ASTM International: *ASTM E8: Annual Book of ASTM Standards 4*, West Conshohocken, ASTM International, 2010, pp. 1–27.
22. W.F. Savage and C.D. Lundin: *Weld. Res. Suppl.*, 1965, vol. 44, pp. 433–42.
23. J.C. Lippold and W.F. Savage: *Weld. J. (Miami Fla)*, 1982, vol. 61, pp. 388–96.
24. P. Nash and A. Nash: *Bull. Alloy Phase Diagr.*, 1987, vol. 8, pp. 6–14.
25. G.A. Knorovsky, M.J. Cieslak, T.J. Headley, A.D. Romig, and W.F. Hammett: *Metall. Trans. A*, 1989, vol. 20A, pp. 2149–58.
26. I.D. Choi, D.K. Matlock, D.L. Olson, and E. Procedures: *Scripta Metall.*, 1988, vol. 22, pp. 1563–68.
27. J.N. Dupont, C.V. Robino, A.R. Marder, and M.R. Notis: *Metall. Mater. Trans. A*, 1998, vol. 29A, pp. 2797–2806.
28. M.J. Cieslak, T.J. Headley, G.A. Knorovsky, A.D. Romig, and T. Kollie: *Metall. Trans. A*, 1990, vol. 21, pp. 479–88.
29. J.N. DuPont, J.R. Michael, and B.D. Newbury: *Welding Metallurgy of Alloy HR-160 (No. SAND99-1355J)*, Albuquerque, NM and Livermore, CA, 1999.
30. V. Biss and D.L. Sponseller: *Metall. Trans.*, 1973, vol. 4, pp. 1953–60.
31. J.N. DuPont, J.C. Lippold, and S.D. Kiser: *Welding Metallurgy and Weldability of Nickel-Base Alloys*, Wiley, Hoboken, 2009.
32. L. Jia, H. Xie, Z.L. Lu, X. Wang, and X. Lin: *Mater. Sci. Technol. (UK)*, 2013, vol. 29, pp. 995–99.
33. H. Xie, L. Jia, and Z. Lu: *Mater. Charact.*, 2009, vol. 60, pp. 114–18.
34. Q. Lei, Z. Li, T. Xiao, Y. Pang, Z.Q. Xiang, W.T. Qiu, and Z. Xiao: *Intermetallics*, 2013, vol. 42, pp. 77–84.
35. J.O. Andersson, T. Helander, L. Höglund, P.F. Shi, and B. Sundman: *Calphad*, 2002, vol. 26, pp. 273–312.
36. *Thermo-Calc TCBIN Bin. Solut. Database*. Accessed Jan 2023.
37. N.F. Lashko, K.P. Sorokina, and A.N. Gorbunov: *Termicheskaya Obrab. Met.*, 1966, vol. 8, pp. 485–87.
38. Y. Mo, D. Wang, B. Jiang, Y. Li, H. Liu, C. Wang, X. Cai, and J. Wang: *Adv. Eng. Mater.*, 2016, vol. 18, pp. 1453–59.
39. Y. Mo, D. Wang, H. Liu, Q. He, G. Huang, B. Jiang, and J. Song: *Mater. Res. Express*, 2019, <https://doi.org/10.1088/2053-1591/ab109a>.
40. S.Z. Han, J.H. Gu, J.H. Lee, Z.P. Que, J.H. Shin, S.H. Lim, and S.S. Kim: *Met. Mater. Int.*, 2013, vol. 19, pp. 637–41.
41. J. Zou, J. Cheng, G. Feng, J. Xie, and F. Yu: *Metals (Basel)*, 2019, vol. 9, pp. 1–13.
42. P. Zhang, X. Liu, and H. Yan: *Surf. Coat. Technol.*, 2017, vol. 332, pp. 504–10.
43. Y. Mishima, S. Ochiai, N. Hamao, and M. Yodogawa: *Trans. Jpn Inst. Met.*, 1986, vol. 27, pp. 656–64.
44. H.A. Roth, C.L. Davis, and R.C. Thomson: *Metall. Mater. Trans. A*, 1997, vol. 28A, pp. 1329–35.
45. Z. Tianxiang, L. Yundong, Z. Zhi, and Z. Yaoxiao: *MRS Proc.*, 1990, vol. 213, pp. 137–42.
46. S. Floreen, G.E. Fuchs, and W.J. Yang: *Miner. Met. Mater. Soc.*, 1994, vol. 718, pp. 13–37.
47. A.K. Bhambri, T.Z. Kattamis, and J.E. Morral: *Metall. Trans. B*, 1975, vol. 6, pp. 523–37.
48. Z.-H. Yu, L. Liu, X.B. Zhao, W.G. Zhang, J. Zhang, and H.Z. Fu: *Trans. Nonferr. Met. Soc. China (Engl. Ed.)*, 2010, vol. 20, pp. 1835–40.
49. A. E. Fraser: *Masters Thesis*, 2019, pp. 1–76.
50. S. Kou: *Acta Mater.*, 2015, vol. 88, pp. 366–74.
51. N.L.M. Veldman, A.K. Dahle, D.H. Stjohn, and L. Arnberg: *Metall. Mater. Trans. A*, 2001, vol. 32A, pp. 147–55.
52. T.W. Clyne and G.J. Davies: *Br. Foundrymen*, 1981, vol. 74, pp. 65–73.
53. M.A. Easton, M.A. Gibson, S. Zhu, and T.B. Abbott: *Metall. Mater. Trans. A*, 2014, vol. 45A, pp. 3586–95.
54. D.J.M. King, M. Yang, T.M. Whiting, X. Liu, and M.R. Wenman: *Acta Mater.*, 2020, vol. 183, pp. 350–61.

**Publisher's Note** Springer Nature remains neutral with regard to jurisdictional claims in published maps and institutional affiliations.

Springer Nature or its licensor (e.g. a society or other partner) holds exclusive rights to this article under a publishing agreement with the author(s) or other rightsholder(s); author self-archiving of the accepted manuscript version of this article is solely governed by the terms of such publishing agreement and applicable law.